Photoacoustic oximetry imaging performance evaluation using dynamic blood flow phantoms with tunable oxygen saturation

WILLIAM C. VOGT,[*] XUEWEN ZHOU, RUDY ANDRIANI, KEITH A. WEAR, T. JOSHUA PFEFER, AND BRIAN S. GARRA

Center for Devices and Radiological Health, U.S. Food and Drug Administration, 10903 New Hampshire Avenue, Silver Spring, MD 20993, USA
*william.vogt@fda.hhs.gov

Abstract: Multispectral photoacoustic oximetry imaging (MPOI) is an emerging hybrid modality that enables the spatial mapping of blood oxygen saturation (SO_2) to depths of several centimeters. To facilitate MPOI device development and clinical translation, well-validated performance test methods and improved quantitative understanding of physical processes and best practices are needed. We developed a breast-mimicking blood flow phantom with tunable SO_2 and used this phantom to evaluate a custom MPOI system. Results provide quantitative evaluation of the impact of phantom medium properties (Intralipid versus polyvinyl chloride plastisol) and device design parameters (different transducers) on SO_2 measurement accuracy, especially depth-dependent performance degradation due to fluence artifacts. This approach may guide development of standardized test methods for evaluating MPOI devices.

1. Introduction

1.1 Multispectral photoacoustic oximetry imaging

Photoacoustic imaging (PAI) is a rapidly emerging hybrid modality that combines pulsed optical excitation with acoustic detection to achieve imaging with both the high contrast of optical imaging and the deep tissue penetration afforded by ultrasound imaging [1]. One of the most powerful features of PAI is the use of tunable light sources to perform multispectral imaging, which enables measurement of both spatial distribution and spectral signature of endogenous chromophores (e.g., hemoglobin) as well as exogenous contrast agents (e.g., dyes, nanoparticles). Most notably, by spectrally detecting relative quantities of oxyhemoglobin (HbO_2) and deoxyhemoglobin (Hb), multispectral PAI can be used to generate maps of blood oxygen saturation (SO_2), which is an invaluable physiological parameter for detecting, diagnosing, and treating disease, especially cancer [2,3]. Clinical applications of multispectral photoacoustic oximetry imaging (MPOI) include breast cancer detection [4–6], cerebral oximetry [7], and thermal therapy monitoring [8]. Additionally, MPOI has been proposed as a preclinical assessment tool for studying animal models of cancer [9–11], functional cerebrovascular hemodynamics [12], and vascular responses to therapeutic cancer drugs [13].

1.2 Standardized performance test methods

There are myriad challenges to overcome as a medical technology is developed and undergoes clinical translation. The lack of well-validated standardized performance test methods is a significant barrier to rapid translation and maturation of optical imaging and spectroscopy devices [14]. This is especially true for PAI devices because: 1) PAI employs complex hybrid mechanisms requiring careful consideration/replication of both optical and acoustic effects in performance tests, 2) PAI is being investigated for many different

applications, resulting in wide variation in device configurations and parameters that may necessitate different types of testing (e.g., linear-array vs. circular scanning systems, optical wavelengths, acoustic frequency range), and 3) there are currently no FDA-approved PAI-based medical devices, although there is a growing number of commercially available devices for preclinical research and exploratory clinical use [15–19]. There is a current need to develop standardized performance test methods so that as PAI technology matures, well-validated approaches are available to streamline many parts of the product life cycle including device development and optimization, inter-device comparison, regulatory decision-making, quality assurance and quality control, maintenance and constancy testing, user training, regulatory evaluation, standardization, and accreditation.

Mature medical imaging technologies such as ultrasound, X-ray computed tomography, and magnetic resonance imaging have already overcome translation barriers, and thus provide a roadmap towards standardization of biophotonics-based devices. Testing using tissue-mimicking phantoms is a cornerstone of performance testing for mature imaging modalities, and their use in performance testing is often prescribed in international standards, consensus documents, and accreditation programs [20,21]. Standards have been developed for biophotonics technologies including pulse oximetry [22] and optical coherence tomography [23,24], and the existence of such standards can provide an indicator that a technology has reached maturity.

Image quality should be considered a fundamental aspect of PAI device performance. However, the accuracy of functional parameters derived from spectral measurements (e.g., SO_2) is also an essential feature that requires quantitative validation. Quantitative multispectral PAI is challenging due to 'spectral coloring' artifacts caused by spatial- and wavelength-dependent fluence distribution in tissue, where target photoacoustic spectra are filtered by background tissue absorption and scattering [25]. The development of fluence correction algorithms and strategies remains an active area of research [26–29]. We previously developed novel tissue-mimicking materials based on polyvinyl chloride plastisol (PVCP) and demonstrated their utility for phantom-based image quality testing of PAI systems [30–32]. However, while these phantoms were biologically relevant, only single-wavelength imaging was evaluated. There is thus an outstanding need to develop phantom-based performance test methods for MPOI devices that specifically enable quantitative assessment of SO_2 measurement accuracy.

1.3 Review of optical oximetry device performance testing

To develop performance test methods for MPOI, we first considered previous works by others describing performance testing for photoacoustic and other optical oximetry techniques, for which there is extensive literature on bench test methods. Pulse oximetry is the most mature and ubiquitous biophotonics-based medical device, and an International Organization of Standardization (ISO) standard has been developed which describes performance testing recommendations [22]. This standard also establishes an acceptance criterion of ≤ 4% root-mean-square difference (RMSD) between pulse oximeter and 'gold standard' CO-oximetry measurements over the range of SO_2 values claimed to be accurate. Early studies described blood flow circuits comprised of a roller pump to induce highly controlled pulsatile flow (a requirement for most pulse oximeters) and an oxygenator to adjust blood SO_2 [33]. However, phantoms were generally simple, consisting of a single fluid channel in a background medium with unspecified optical properties and thus uncertain biological relevance. Kurth et al. developed a near-infrared spectroscopy (NIRS) device test method incorporating a brain phantom with sub-millimeter channels containing flowing blood, with adjustable SO_2 via a membrane oxygenator [34]. Another common approach is to use turbid liquid phantoms, such as Intralipid-hemoglobin solutions [35–37]. More recently, a liquid phantom for NIRS tissue oximeter evaluation was developed that includes electrodes for measuring partial pressures of O_2 and CO_2 as well as pH [38]. However, such liquid phantoms lack temporal stability and

are necessarily homogeneous, limiting their suitability for testing MPOI devices, as phantoms would generally require stable embedded inclusions with different optical absorption than the background.

Several studies have described oximetry performance testing of photoacoustic devices intended for applications such as cuvette spectroscopy, preclinical animal imaging, and clinical oximetry [25,39–43]. These previous studies illustrated many different approaches ranging from testing in ex vivo tissues to blood flow phantoms containing a small number of fluid channels. However, several general limitations in methods or findings were identified: 1) tissue phantom optical and acoustic properties were often not characterized or were not biologically relevant, 2) test methods using ex vivo tissues as phantoms lack reproducibility, and 3) most prior test and phantom designs were not suitable for near-infrared, deep-tissue MPOI devices. Our intent is to combine the best aspects of these previous approaches to produce a robust test method suitable for characterizing performance of near-infrared multispectral MPOI systems intended for deep-tissue imaging applications such as breast cancer detection and diagnosis.

1.4 Study objectives

Our overall goal is to address the need for well-validated phantom-based performance test methods for MPOI devices. In this study, our objectives were to develop a breast-mimicking blood flow phantom with dynamically tunable SO_2 and an associated test method. We applied this test method towards evaluation of SO_2 measurement accuracy for a custom MPOI device and investigated the impact of tissue properties and device design parameters on device performance. Our emphasis was on developing test methodology for device performance assessment, rather than developing methods for optimal design of MPOI device features such as fluence correction algorithms.

2. Methods

2.1 Blood flow circuit

Figure 1 shows a schematic of the blood flow circuit used to achieve dynamically adjustable SO_2. The circuit included a blood reservoir, a membrane oxygenator comprised of a bundle of porous hollow fibers (PermSelect, MedArray, Inc., Ann Arbor, MI), and a peristaltic pump (Masterflex L/S, Cole-Parmer, Inc., Vernon Hills, IL). A mixture of oxygen and nitrogen gas was delivered through the lumina of the hollow fibers for exchange with flowing blood (deoxygenation: 1.6 LPM N_2 and 0 LPM O_2; oxygenation: 1.55 LPM N_2 and 0.05 LPM O_2). The membrane oxygenator was oriented so that blood flowed around the fibers and against gravity (to remove bubbles and froth) and gas flowed with gravity to provide efficient counterflow mass transfer. A custom acrylic housing was built to allow insertion of pH, temperature, and dissolved oxygen (DO) probes for real-time inline flow measurements of SO_2. Once the blood circuit reached a desired SO_2 value, the membrane oxygenator gas line was sealed, which stabilized blood SO_2 for at least 1 hour. After drawing 200 µL to clear old blood within the sample port, 200 µL blood samples were drawn before and after image acquisition for CO-oximetry measurements. A clinical grade CO-oximeter (Avoximeter 4000, Accriva Diagnostics, Inc., San Diego, CA) served as a reference device and provided gold-standard measurements of blood SO_2 and total hemoglobin (tHb), as well as fractional Hb, HbO_2, methemoglobin, and carboxyhemoglobin.

Bench performance test methods should possess the minimum complexity needed to provide test results that are adequate for device design, evaluation, and validation. We simplified our blood flow phantom by omitting CO_2 gas delivery and conducted testing at room temperature. As will be shown in the results, adequate calibration of DO electrodes against a clinical-grade CO-oximeter produced accurate SO_2 tuning. DO electrode measurements were calibrated to SO_2 values by tuning circuit oxygenation to several levels,

recording DO, then drawing blood for CO-oximetry. Thus, DO readings could be used as a real-time surrogate for SO_2 to facilitate accurate tuning.

Red blood cell (RBC) suspensions were prepared from whole defibrinated bovine blood (Quad Five, Inc., Ryegate, MT) as described by Laufer et al. [40]. 10 U/mL of heparin (H3149, Sigma Aldrich, Inc., Allentown, PA) was added to the blood, which was then centrifuged at 3000 RPM for 10 minutes to separate RBCs from the plasma and buffy coat. Plasma was aspirated and RBCs were suspended in phosphate buffer saline (PBS, pH 7.3) and centrifuged twice. From CO-oximetry, suspension tHb was 13.5 ± 1.0 g/dL, which is representative of average tHb in healthy women (12-16 g/dL) [44]. Bovine and human hemoglobin are known to have nearly identical extinction spectra [45].
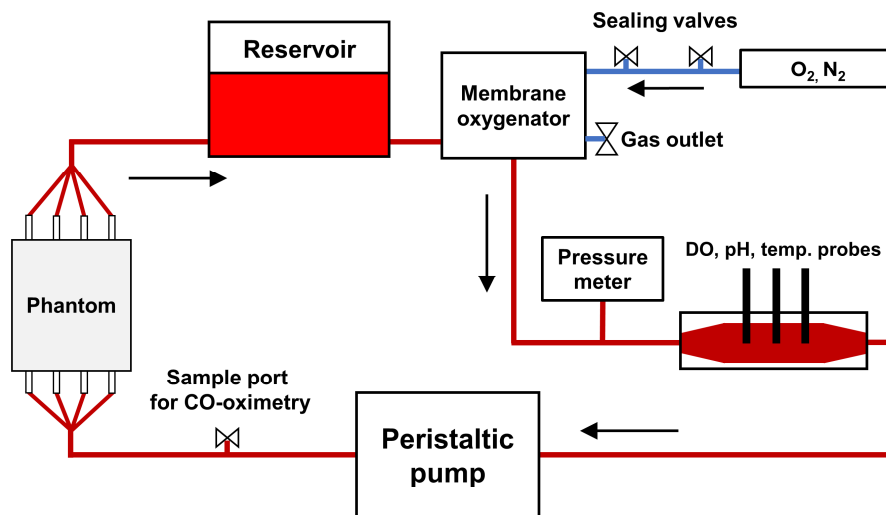

Fig. 1. Schematic of blood flow circuit showing key components [46].

2.2 Tissue-mimicking phantoms

Several tissue-mimicking materials have been developed for fabricating photoacoustic imaging phantoms, including gelatin [47], PVA cryogels [48], and gel wax [49] (see [30] for a detailed review of photoacoustic tissue-mimicking materials). To evaluate impact of phantom background material selection on test method results, we investigated both a simple liquid phantom comprised of 1% Intralipid (I141, Sigma-Aldrich, Inc.) and a breast-mimicking polyvinyl chloride plastisol (PVCP) phantom with biologically relevant optical and acoustic properties [30–32]. Phantom optical properties were determined by molding four disk-shaped samples with 5 mm thickness and 38.4 mm diameter, then measuring diffuse reflectance and transmittance using integrating sphere spectrophotometry. Optical absorption and reduced scattering coefficients were calculated from these data using the well-known inverse adding-doubling algorithm [50]. PVCP properties show general agreement with literature data on breast optical properties (Fig. 2) [51]. Because the very low optical absorption of Intralipid affects accuracy of this spectrophotometry method, 1% Intralipid solution was assumed to have optical absorption spectrum of water and reduced optical scattering coefficient spectrum from literature data [52].

For each medium tested (Intralipid and PVCP), the material was poured into a 7 cm x 7 cm x 5 cm acrylic mold containing seven suspended polytetrafluoroethylene (PTFE) tubes (1.07 mm inner diameter, STT-18, Component Supply Company, Fort Meade, FL) at depths

from 5 to 35 mm, with 2.5 mm lateral spacing (Fig. 3). PVCP was prepared as described previously [30], then poured through a side channel while the mold face corresponding to the imaging surface was covered with an aluminum plate. This maintained an even surface and prevents sag during curing. Spray foam sealant (LOCTITE Tite foam, Henkel Corp., Rocky Hill, CT) was applied to the tube roots external to the mold chamber to prevent bending. Tube ends were bundled with modeling clay and super glue and inserted into 4.8 mm inner diameter tubes that included quick-connect fittings for rapid phantom installation into the blood flow circuit as well as easy removal for cleaning (PMC1703, PMC2204, Qosina, Ronkonkoma, NY).
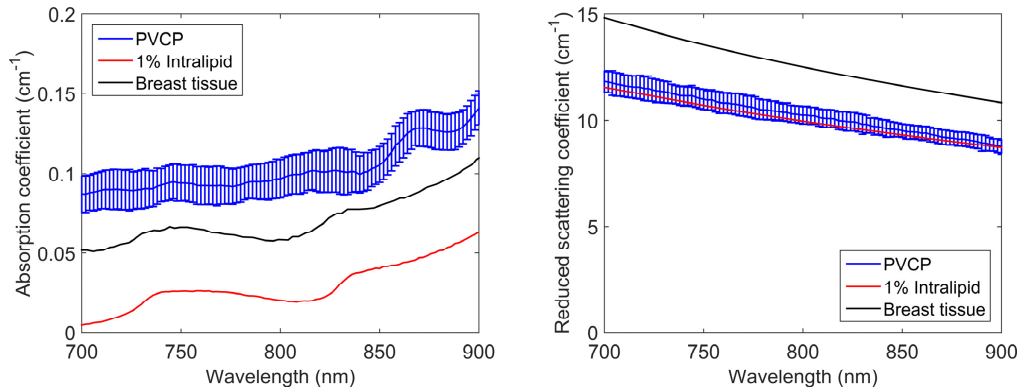

Fig. 2. Optical properties of 1% Intralipid and PVCP phantoms. Error bars for PVCP represent one standard deviation. Breast tissue literature values from Pifferi et al. [51].
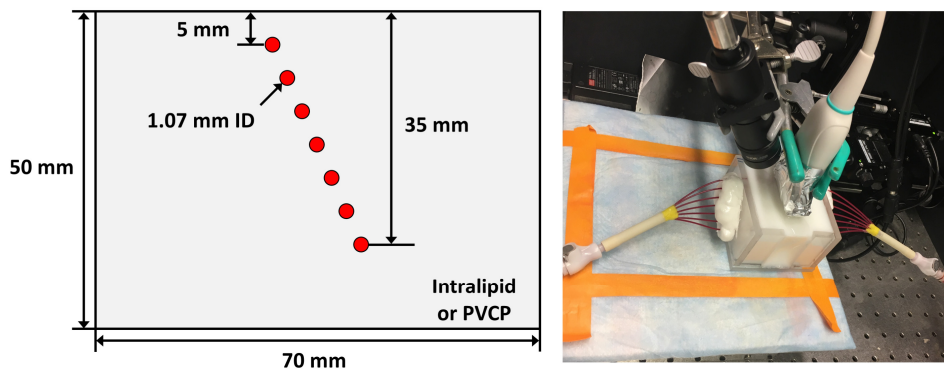

Fig. 3. Left: Tissue phantom geometry, showing blood-filled tubes at several depths. Transducer is placed at the top surface. Right: PVCP phantom connected to blood flow and placed under PAI transducer assembly [46].

2.3 Custom MPOI system

MPOI was performed using a custom PAI system described previously [30,31]. Briefly, the system consisted of a rapidly tunable NIR optical parametric oscillator (OPO) (Phocus Mobile, Opotek, Inc. Carlsbad, CA) and a 128-channel ultrasound system (Vantage 128, Verasonics, Inc., Seattle, WA). Image acquisition, real-time display, reconstruction, and post-processing were performed using Matlab (The Mathworks, Inc., Natick, MA). The OPO emitted 5 ns pulses at a 10 Hz pulse repetition rate and included a fast-tuning module that enabled per-pulse wavelength tuning over 690-950 nm. An internal energy sensor was used to correct images for pulse energy variation and wavelength-dependent laser energy output. An engineered line-pattern diffuser was used to convert the output of a circular fiber bundle to a 5 mm x 35 mm elliptical beam adjacent to the transducer. Total input pulse energy was ~15-19

mJ, and the radiant exposure over all wavelengths was 8-10 mJ/cm^2, which is below the wavelength-dependent maximum permissible exposure established by the American National Standards Institute (ANSI) [53]. Photoacoustic signals were detected using either an 8 MHz or 2.5 MHz transducer array mounted on a 3D motorized stage (L11-4v, Verasonics; ATL P4-1, Priority Medical Inc., Greenbrier, TN) (Table 1). Transducers were covered with ultrasound gel-coupled aluminum foil to reduce unwanted photoacoustic signal generation on the transducer surface by diffusely reflected light. Received acoustic signals were amplified by 82 dB, low-pass filtered, then digitized for image reconstruction using a proprietary real-time reconstruction algorithm provided by Verasonics.

Table 1. Transducer parameters and performance characteristics

	Center Frequency (MHz)	Bandwidth (MHz)	Element pitch (mm)	Array length (mm)	Array width (mm)	Axial resolution (mm)	Lateral resolution (mm)
L11-4v	8.0	8.7	0.300	38.4	12	~0.25	~0.6
P4-1	2.5	2.2	0.295	28.3	20	~0.8	~1.0

2.4 Imaging experiments and data processing

Phantoms were connected to the flow circuit, aligned to the imaging assembly, then flushed with 1X PBS for 30 minutes. After draining PBS, RBC suspensions were infused into the circuit and air bubbles were removed. Blood temperature and pH were observed to be stable within $22 \pm 1°C$ and 7.45 ± 0.1, respectively. The circuit was initially infused with oxygen to achieve near-complete saturation, then stepped down to lower SO_2 levels. After CO-oximetry sampling, MPOI was performed for SO_2 setpoints from ~99% to 30% in 10% intervals. To better elucidate wavelength-dependence of MPOI performance, especially in the presence of fluence artifacts, 'hyperspectral' scans were acquired using 76 wavelengths (700 to 850 nm in 2 nm increments). Ten complete scans were acquired per SO_2 setpoint.

Photoacoustic spectra were computed by selecting a rectangular region of interest (ROIs) around a target tube, then applying a mask to remove pixels below 50% of ROI maximum pixel intensity as performed in our previous studies [30,31]. ROIs were 10 x 8 pixels (depth x width), with dimensions of 1.18 x 2.40 mm and 2.95 x 2.37 mm for the L11-4v and P4-1 arrays, respectively. This allowed isolation of the proximal and distal tube edges while discarding the lumen and surrounding regions, which do not carry blood-based photoacoustic signals. Spectral signal quality was summarized by computing coefficient of variation (COV, ratio of standard deviation to mean) per wavelength over 10 scans, then averaging COV values over all wavelengths.

Spectra were corrected for fluence variation with both depth and wavelength using a heuristic 1D fluence model based on the diffusion approximation for a uniform infinitely wide beam exposure [29,54]:

$$\Phi(z,\lambda) = e^{-z\sqrt{3\mu_a(\lambda)(\mu_a(\lambda)+\mu_s'(\lambda))}} \tag{1}$$

where Φ is depth- and wavelength-dependent fluence, z is depth, λ is optical wavelength, and $\mu_a(\lambda)$ and $\mu_s'(\lambda)$ are the absorption and reduced scattering spectra of PVCP or Intralipid. This simple correction serves to provide some method of fluence compensation in the MPOI device being evaluated by our developed test method, as this is a common feature of such devices. Our objective was to demonstrate utility of the developed test method for MPOI performance assessment, rather than to use the test method to optimize design aspects of a specific device. SO_2 was computed from fluence-corrected spectra per pixel using nonnegative least-squares unmixing using all scanned wavelengths, assuming presence of only oxyhemoglobin and deoxyhemoglobin [40]. SO_2 maps were thresholded based on total

hemoglobin (tHb) maps to avoid display of oximetry information for weak background pixels. Average background tHb was computed from ROIs adjacent to tube ROIs, multiplied by 1.5, then interpolated to produce a depth-dependent threshold level. Literature values for hemoglobin extinction coefficient spectra compiled for whole blood were used for spectral unmixing [55]. Following standardized methods for pulse oximeter performance evaluation, SO_2 measurement accuracy was quantified by calculating the RMSD between measured photoacoustic and CO-oximeter SO_2 values:

$$RMSD = \sqrt{\frac{1}{n}\sum_{i=1}^{n}(SO_{2,PA,i} - SO_{2,CO,i})^2}$$
(2)

where n is the number of measurement pairs, $SO_{2,PA,i}$ is the photoacoustic SO_2 measurement, and $SO_{2,CO,i}$ is the CO-oximeter SO_2 measurement [22].

3. Results and discussion

3.1 Blood system tuning performance

The blood flow circuit enabled stable, accurate, and precise SO_2 tuning over the duration of imaging experiments. DO electrode readings were calibrated to SO_2 values from CO-oximetry during three separate tuning experiments (Fig. 4), but the calibrations for deoxygenation and reoxygenation were different. These oxygen dissociation curve shifts may be attributed to the absence of CO_2 gas in our approach, which results in low pCO_2 and reduced pH stability (reversible pH decreases of ~0.1-0.15 were observed) [56]. Tuned SO_2 was accurate within ± 1% when performing fine-tuning based on CO-oximetry measurements, rather than relying solely on DO measurements. The representative temporal tuning response in Fig. 4 illustrates that the set DO level resulting in the intended SO_2 level did not always match the target DO level based on the calibration curve. SO_2 was also demonstrated to be stable within ± 1% for at least 30 minutes for all levels (data not shown). Laufer et al. used a similar membrane oxygenator-based blood flow circuit approach and reported <1% SO_2 variation over 20 minutes at fixed levels, but a higher SO_2 variation of ± 4.1%, the accuracy limit of their CO-oximeter [40]. Mitcham et al. used a simpler method by varying SO_2 by separately bubbling O_2 and N_2 into blood reservoirs, then mixing at various ratios, which achieved broad SO_2 tuning but with higher variation (± 2-3%) [42]. SO_2 tuning speed was moderately fast, taking 5-10 minutes to adjust SO_2 by 10% with no undershoot. For very low SO_2 values, tuning was slower due to several effects that shift the dissociation curve to the left, such as operating at room temperature and low pCO_2. However, the system could still be readily adjusted to SO_2 levels as low as 30%, which is an adequate lower bound to cover the physiologically relevant range of values for normal artery/vein levels (~60-100%). Tuning speed was markedly faster for resaturation than desaturation, either due to faster gas exchange or the apparent left-shift in the resaturation dissociation curve observed through DO electrode calibration.
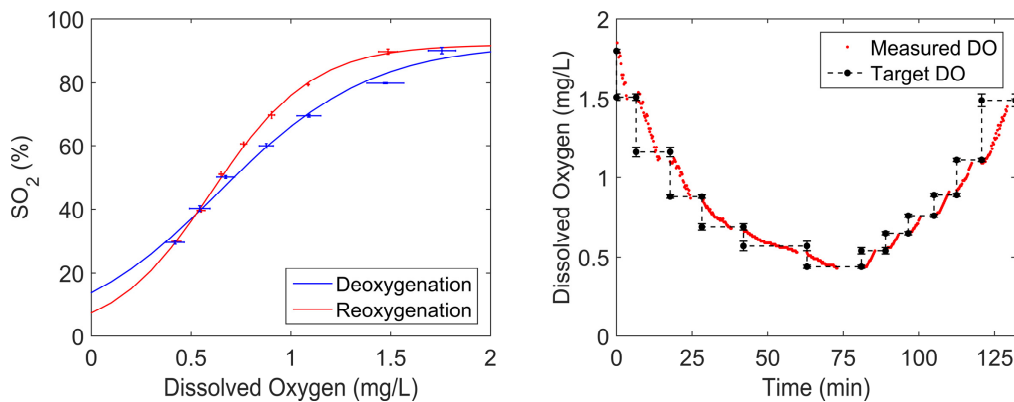
Fig. 4. SO$_2$ tuning performance of the flow circuit. Left) Calibration measurements of DO to SO$_2$ measurements from CO-oximetry. Solid lines denote fitted log-log sigmoid functions. Vertical and horizontal error bars represent three separate tuning experiments. Right) Representative temporal response of DO electrode during experiments. Error bars represent uncertainty in calibrated DO set points (i.e., horizontal blue error bars in the left plot). Gaps in measured data (points) represent imaging periods at constant SO$_2$.

3.2 Impact of phantom properties

3.2.1 Image quality and oximetry mapping

Figure 5 shows representative raw and fluence-corrected single-wavelength, log-compressed images acquired at 800 nm, as well as computed SO$_2$ maps. Fluence correction improved image intensity uniformity with depth and, for a fixed display dynamic range of 40 dB, improved visualization of deeper targets. However, because this correction only rescales the data, the underlying signal-to-noise ratio (SNR) of the image information is not improved, resulting in enhanced background noise in deep regions. Some near-field clutter in the first 5 mm is generated by signals generated on the transducer surface. Additionally, these surface-generated signals can transmit into the phantom and reflect off the embedded tubes, creating image artifacts beneath the tubes (at twice the tube depth due to beamforming assuming one-way propagation). These artifacts are substantially reduced in the PVCP phantom due to higher background optical and acoustic attenuation. Because the spectra of these surface-generated signals are relatively flat compared to the absorption spectrum of deoxyhemoglobin, the unmixing algorithm interprets them as having higher oxyhemoglobin content, resulting in colorization as high SO$_2$. Apart from these reflection artifacts, oximetry maps were shown to adequately suppress image background and prioritize display of the blood-filled fluid channels.

Photoacoustic spectra measured from ROI analysis are shown in Fig. 6, while Fig. 7 shows COV for spectra collected from different target depths and for each imaging scenario. Spectra show expected increases in COV (or equivalently, decreases in SNR) with depth. Spectrum SNR ranged from 2.0 to 133 over all wavelengths, target depths, and imaging experiments. COV was generally higher in Intralipid than PVCP phantoms, which may be due to horizontal electronic scan noise artifacts observed for deeper regions. Measured spectra were strongly affected by spectral corruption artifacts, especially in the Intralipid phantom. This is because Intralipid, while providing biologically relevant scattering, does not provide sufficient optical absorption to adequately simulate tissue. The optical absorption spectrum of Intralipid (assumed to be that of water) is not only low in magnitude, but also has greater relative variation over the NIR window compared to tissue, which results in greater differences in fluence distribution. Heuristic fluence corrections improved agreement between measured spectra and literature spectra for blood, although the improvement was more significant in Intralipid as opposed to PVCP phantom measurements due to greater spectral corruption artifacts observed in Intralipid.
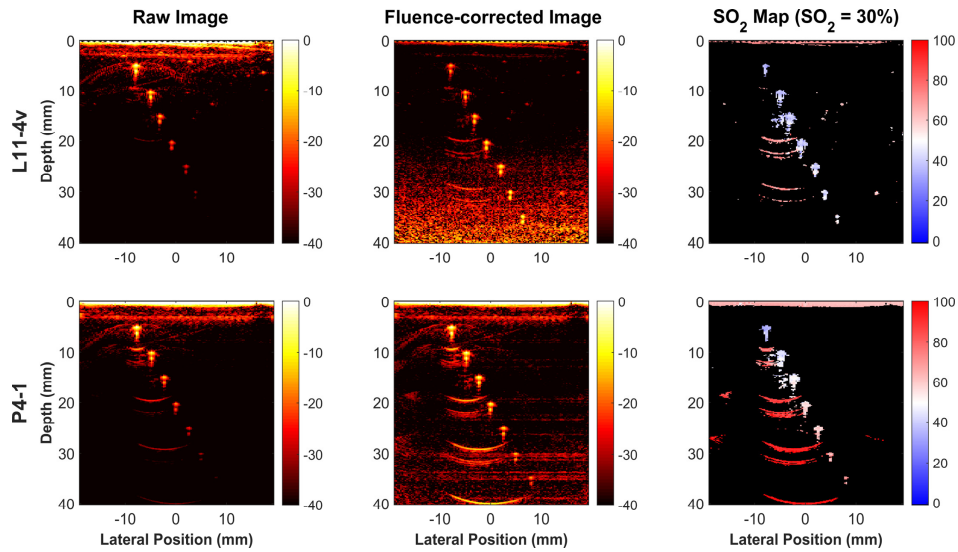
Fig. 5. Representative raw and fluence-corrected photoacoustic images at 800 nm, as well as SO_2 maps for PVCP (top row) and Intralipid (bottom row) phantoms, collected with the L11-4v transducer. Color bars for PA and SO_2 images are in dB and % SO_2, respectively. Each image displayed in dB is normalized to its own maximum intensity below 3 mm.
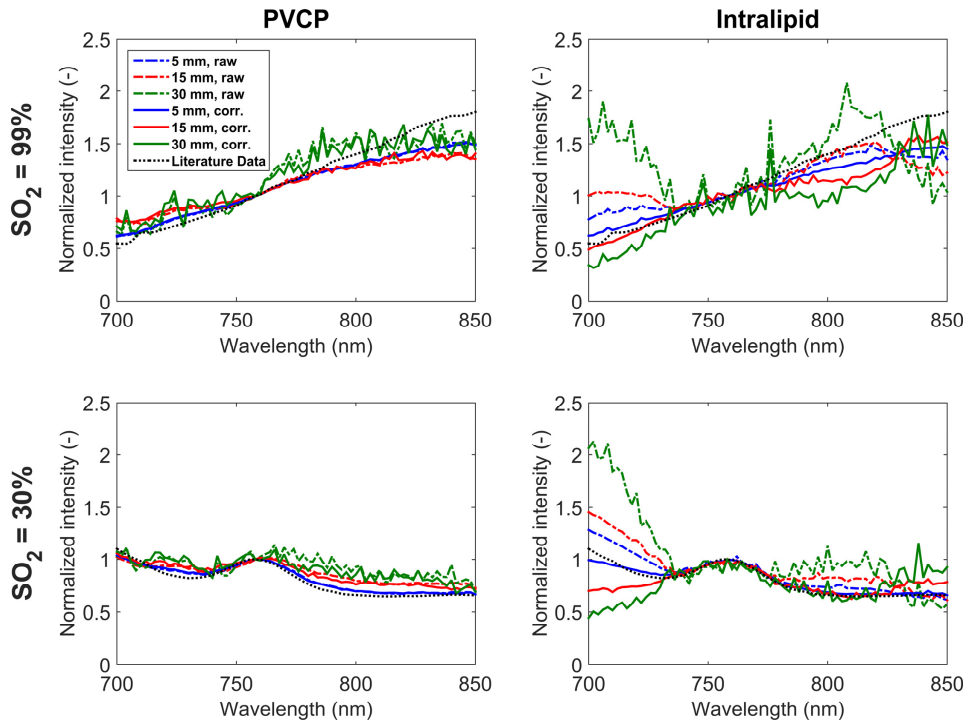

Fig. 6. Comparing raw and fluence-corrected (corr.) photoacoustic spectra vs. depth for PVCP (left column) and Intralipid (right column) phantoms at high SO_2 (top row) and low SO_2 (bottom row), measured with the L11-4v transducer. Error bars omitted for clarity, with uncertainty in spectra summarized by COV data presented in Fig. 7.
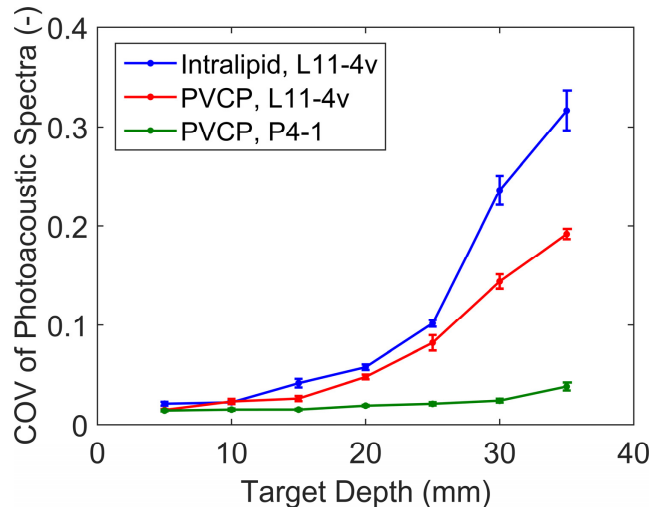
Fig. 7. COV of photoacoustic spectra vs. depth for each imaging scenario. Error bars denote 1 standard deviation over all wavelengths and SO_2 set points.

3.2.2 SO_2 measurement accuracy

Figure 8 shows oximetry maps computed from fluence-corrected images for both Intralipid and PVCP phantoms and for several SO_2 setpoints. Qualitative assessment of the images suggested the predicted SO_2 value does not vary substantially with target depth within each image. However, a closer, quantitative comparison of photoacoustic SO_2 measurements compared to CO-oximetry revealed substantial depth dependence in RMSD for both phantom cases (Fig. 9). In the Intralipid phantom data, a dramatic depth-dependence in SO_2 measurement accuracy was observed, with RMSD as high as 40%. In comparison, fluence-corrected data from the PVCP phantom scenario produced weaker depth-dependence in SO_2 measurement accuracy and RMSD of ~5-7%, which approaches the ISO-defined acceptable performance criterion for pulse oximeters (< 4%) [22].
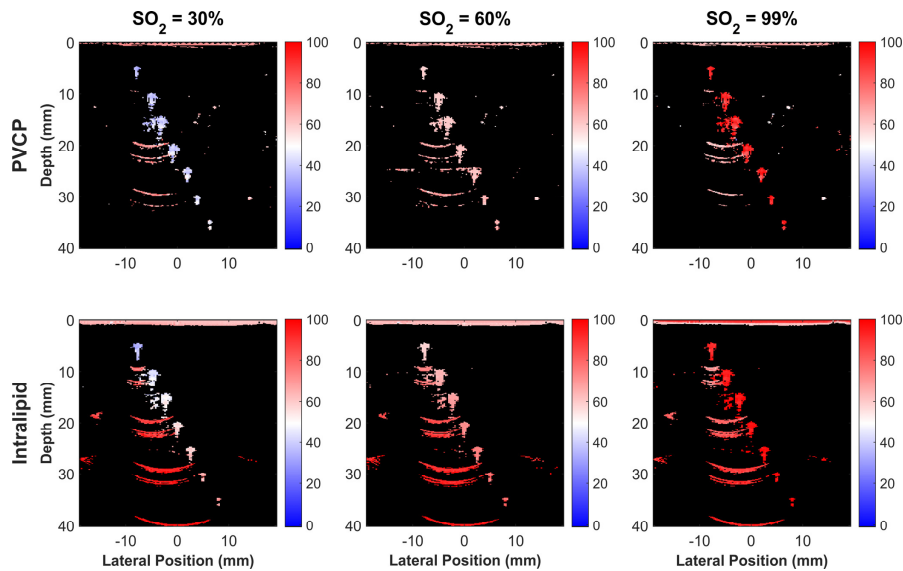

Fig. 8. SO_2 maps for PVCP (top row) and Intralipid (bottom row) phantoms at several SO_2 levels, acquired with the L11-4v transducer. Color bars in units of % SO_2.
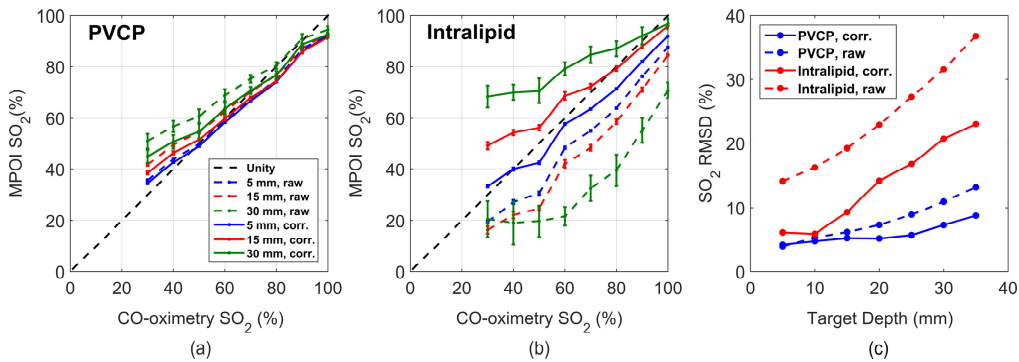
Fig. 9. a-b) MPOI vs. CO-oximetry SO_2 for raw and fluence corrected (corr.) images vs. depth for PVCP (a) and Intralipid (b) phantoms measured with the L11-4v transducer. c) RMSD vs. depth for each scenario. Error bars denote 1 standard deviation.

3.3 Transducer performance comparison

Representative photoacoustic images and oximetry maps collected using the L11-4v and P4-1 transducers are shown in Fig. 10. Targets appear substantially larger in P4-1 images due to reduced axial and lateral resolution (see Table 1). However, these images present much greater target contrast, especially for deep targets, because of greater low-frequency content of photoacoustic signals and reduced acoustic attenuation at lower frequencies. This result is expected given the trade-off between resolution and sensitivity as characterized in our previous work [31]. However, the low acoustic attenuation also results in enhancement of surface-generated reflection artifacts, which is exacerbated by the fluence correction algorithm. Thresholding successfully removed many of these reflections from oximetry maps. It is also apparent that target intensity still varies significantly with depth, despite use of fluence correction. This may be due to discrepancies between the simplified fluence model used for compensation and the actual fluence distribution. No additional depth compensation (i.e. time-gain compensation) was performed to account for acoustic attenuation or possible diffraction/beamforming effects on image intensity depth profiles. Because photoacoustic sources are generally omnidirectional, the finite transducer receive aperture may cause complex depth-dependent reductions in target signal that depend on transducer geometry.

As shown in Fig. 7, spectra acquired with the P4-1 array displayed lower COV than L11-4v array data due to increased signal intensity and SNR, which is consistent with our previous observations [31]. However, the P4-1 transducer generally underestimated SO_2 for values from ~60-100% and produced greater SO_2 errors for shallower targets compared to images from the L11-4v transducer (Fig. 11). The low variance of SO_2 measurements over a relatively low number of scans (N = 10) is likely due to the higher SNR of this array and the constrained nature of spectral unmixing when using many wavelengths. Also, fluence correction did not substantially decrease SO_2 RMSD for the P4-1 transducer as compared to L11-4v data. This may be due to the limited accuracy of the heuristic fluence correction, which assumes a laterally infinite uniform illumination. Because the P4-1 array is much wider in the elevational direction than the L11-4v (20 mm vs. 12 mm, Table 1), the elliptical beam is offset by a greater elevational distance from the image plane. Thus, the 'slice' of the 3D fluence distribution coinciding with the image plane is expected to differ significantly from that predicted by our fluence model. This is expected to have greatest impact in shallow tissue regions where fluence would decrease most rapidly with elevational offset from the beam, which may explain reduced SO_2 accuracy for shallow targets using the P4-1 array.
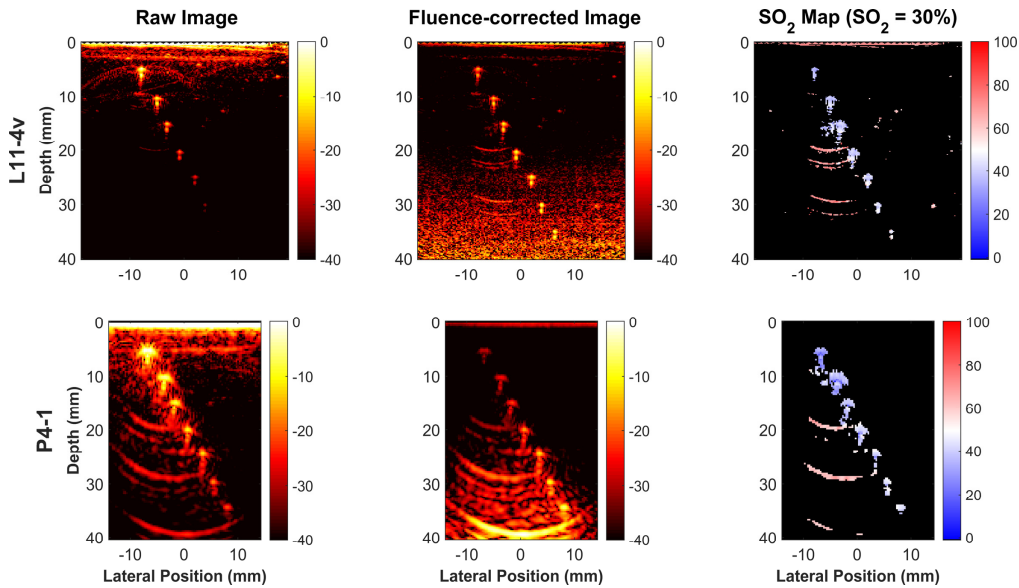
Fig. 10. Representative raw and fluence-corrected photoacoustic images of the PVCP phantom at 800 nm, as well as SO_2 maps acquiring using the L11-4v (top row) and P4-1 (bottom row) transducers. Color bars for PA and SO_2 images are in dB and % SO_2, respectively. Each image displayed in dB is normalized to its own maximum intensity below 3 mm.
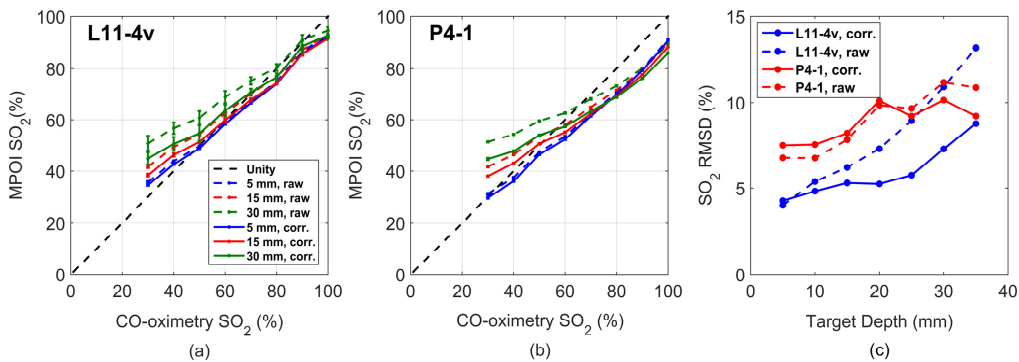

Fig. 11. a-b) MPOI vs. CO-oximetry SO_2 for raw and fluence corrected (corr.) images vs. depth for L11-4v (a) and P4-1 (b) transducers, measured in PVCP phantoms. c) RMSD as a function of depth for each scenario. Error bars denote 1 standard deviation over 10 scans.

4. Discussion and conclusion

Our test results indicated that the developed test method produced accurate, adjustable blood SO_2 in tissue-mimicking phantoms, and that reasonable SO_2 measurement accuracy could be achieved by our custom MPOI device after accounting for tissue optical properties through fluence correction. While we achieved SO_2 RMSD of ~4-14% across different imaging scenarios, Laufer et al. reported SO_2 accuracy of 2.5-4% using a photoacoustic sensor technique in a blood flow cuvette phantom. However, the cuvette did not produce spectral coloring artifacts expected in turbid tissues. Mitcham et al. reported accuracy of 3-15% in measurements of blood-filled tubes an ex vivo bovine prostate phantom depending on use of fluence correction and different unmixing methods. Our results also showed significant improvements in SO_2 accuracy after fluence correction, although SO_2 accuracy was not as high as that reported by Mitcham et al. This may be because they adaptively fitted a fluence model to optimize SO_2 accuracy, while we used a simple, fixed-parameter fluence model based on phantom optical property measurements. Also, rather than investigating the optimal

selection of unmixing wavelengths, we chose to use all measured wavelengths from 700 to 850 nm. Both tissue and PVCP present greater absorption above ~850 nm (in tissue, this is due to water and lipids), a confounding factor that would generate significant spectral coloring artifact. By removing wavelengths for which fluence corrections were less reliable, SO_2 accuracy may have been improved. Optimal wavelength selection is a complex design problem beyond the scope of this study but has been explored by others [57]. Test results illustrated that choice of phantom material produced differences in SO_2 measurement accuracy, and that careful design of phantom optical properties (especially their spectral variation and associated fluence correction algorithms) is an important consideration in design of a MPOI performance test method.

Previous studies have demonstrated that changes in illumination geometry can impact photoacoustic image quality due to differences in fluence profile within the image plane. Held et al. demonstrated that elevational offset of the optical beam modified contrast in near-field forearm tissue and observed optimal image contrast for an offset of 5 mm [58]. Daoudi et al. built a handheld probe with a 2 mm elevational offset between transducer array and optical beam and varied transducer standoff distance from the tissue surface to optimize beam alignment and image quality [59]. Lastly, Sangha et al. built a linear-array PAI system with adjustable optical beam geometry, with results illustrating that adjusting focal depth (which included varying elevational offset) led to improved image quality for given depth ranges [60]. However, these studies did not investigate the impact of beam geometry design and resultant fluence distributions on multispectral measurements and spectral coloring artifacts as elucidated in this work. Fluence correction algorithms should be closely tailored to a given system design, as algorithm performance may be highly sensitive to uncertainty in tissue properties and device design parameters. Future work will include investigation of robust fluence correction models that more accurately simulate complex beam geometries such as offset noncircular beams, which are commonly employed in clinical PAI [61].

In conclusion, we have developed and validated a test method based on a dynamic blood flow phantom that is suitable for characterizing SO_2 measurement accuracy of MPOI systems. Results provide key insights into the impact of tissue properties and system design on performance and highlight the critical role that fluence corrections play in multispectral PAI. This test platform may serve as a foundation for future standardized MPOI performance test methods.

Funding

Disclaimer

The mention of commercial products, their sources, or their use in connection with material reported herein is not to be construed as either an actual or implied endorsement of such products by the Department of Health and Human Services.

Disclosures

WCV: U.S. Dept. of Health and Human Services (P), KAW: U.S. Dept. of Health and Human Services (P), TJP: U.S. Dept. of Health and Human Services (P), BSG: U.S. Dept. of Health and Human Services (P).

References

1. L. V. Wang and S. Hu, "Photoacoustic tomography: in vivo imaging from organelles to organs," Science **335**(6075), 1458–1462 (2012).
2. P. Vaupel, F. Kallinowski, and P. Okunieff, "Blood flow, oxygen and nutrient supply, and metabolic microenvironment of human tumors: a review," Cancer Res. **49**(23), 6449–6465 (1989).

3. R. A. Cairns, I. S. Harris, and T. W. Mak, "Regulation of cancer cell metabolism," Nat. Rev. Cancer **11**(2), 85–95 (2011).

4. E. I. Neuschler, R. Butler, C. A. Young, L. D. Barke, M. L. Bertrand, M. Böhm-Vélez, S. Destounis, P. Donlan, S. R. Grobmyer, J. Katzen, K. A. Kist, P. T. Lavin, E. V. Makariou, T. M. Parris, K. J. Schilling, F. L. Tucker, and B. E. Dogan, "A Pivotal Study of Optoacoustic Imaging to Diagnose Benign and Malignant Breast Masses: A New Evaluation Tool for Radiologists," Radiology **287**(2), 398–412 (2018).

5. M. Toi, Y. Asao, Y. Matsumoto, H. Sekiguchi, A. Yoshikawa, M. Takada, M. Kataoka, T. Endo, N. Kawaguchi-Sakita, M. Kawashima, E. Fakhrejahani, S. Kanao, I. Yamaga, Y. Nakayama, M. Tokiwa, M. Torii, T. Yagi, T. Sakurai, K. Togashi, and T. Shiina, "Visualization of tumor-related blood vessels in human breast by photoacoustic imaging system with a hemispherical detector array," Sci. Rep. **7**(1), 41970 (2017).

6. G. Diot, S. Metz, A. Noske, E. Liapis, B. Schroeder, S. V. Ovsepian, R. Meier, E. Rummeny, and V. Ntziachristos, "Multispectral Optoacoustic Tomography (MSOT) of Human Breast Cancer," Clin. Cancer Res. **23**(22), 6912–6922 (2017).

7. I. Y. Petrova, Y. Y. Petrov, R. O. Esenaliev, D. J. Deyo, I. Cicenaite, and D. S. Prough, "Noninvasive monitoring of cerebral blood oxygenation in ovine superior sagittal sinus with novel multi-wavelength optoacoustic system," Opt. Express **17**(9), 7285–7294 (2009).

8. P. V. Chitnis, H. P. Brecht, R. Su, and A. A. Oraevsky, "Feasibility of optoacoustic visualization of high-intensity focused ultrasound-induced thermal lesions in live tissue," J. Biomed. Opt. **15**(2), 021313 (2010).

9. K. E. Wilson, S. V. Bachawal, L. Tian, and J. K. Willmann, "Multiparametric spectroscopic photoacoustic imaging of breast cancer development in a transgenic mouse model," Theranostics **4**(11), 1062–1071 (2014).

10. M. Gerling, Y. Zhao, S. Nania, K. J. Norberg, C. S. Verbeke, B. Englert, R. V. Kuiper, A. Bergström, M. Hassan, A. Neesse, J. M. Löhr, and R. L. Heuchel, "Real-time assessment of tissue hypoxia in vivo with combined photoacoustics and high-frequency ultrasound," Theranostics **4**(6), 604–613 (2014).

11. M. Priya, B. S. Satish Rao, S. Chandra, A. Datta, S. G. Nayak, and K. K. Mahato, "Monitoring breast tumor progression by photoacoustic measurements: a xenograft mice model study," J. Biomed. Opt. **20**(10), 105002 (2015).

12. M. Li, J. T. Oh, X. Y. Xie, G. Ku, W. Wang, C. Li, G. Lungu, G. Stoica, and L. V. Wang, "Simultaneous Molecular and Hypoxia Imaging of Brain Tumors In Vivo Using Spectroscopic Photoacoustic Tomography," Proc. IEEE **96**(3), 481–489 (2008).

13. J. Laufer, P. Johnson, E. Zhang, B. Treeby, B. Cox, B. Pedley, and P. Beard, "In vivo preclinical photoacoustic imaging of tumor vasculature development and therapy," J. Biomed. Opt. **17**(5), 056016 (2012).

14. B. C. Wilson, M. Jermyn, and F. Leblond, "Challenges and opportunities in clinical translation of biomedical optical spectroscopy and imaging," J. Biomed. Opt. **23**(3), 1–13 (2018).

15. H. Zafar, A. Breathnach, H. M. Subhash, and M. J. Leahy, "Linear-array-based photoacoustic imaging of human microcirculation with a range of high frequency transducer probes," J. Biomed. Opt. **20**(5), 051021 (2015).

16. S. E. Bohndiek, S. Bodapati, D. Van De Sompel, S. R. Kothapalli, and S. S. Gambhir, "Development and application of stable phantoms for the evaluation of photoacoustic imaging instruments," PLoS One **8**(9), e75533 (2013).

17. A. Hariri, J. Lemaster, J. Wang, A. S. Jeevarathinam, D. L. Chao, and J. V. Jokerst, "The characterization of an economic and portable LED-based photoacoustic imaging system to facilitate molecular imaging," Photoacoustics **9**, 10–20 (2017).

18. F. Knieling, C. Neufert, A. Hartmann, J. Claussen, A. Urich, C. Egger, M. Vetter, S. Fischer, L. Pfeifer, A. Hagel, C. Kielisch, R. S. Görtz, D. Wildner, M. Engel, J. Röther, W. Uter, J. Siebler, R. Atreya, W. Rascher, D. Strobel, M. F. Neurath, and M. J. Waldner, "Multispectral Optoacoustic Tomography for Assessment of Crohn's Disease Activity," N. Engl. J. Med. **376**(13), 1292–1294 (2017).

19. J. Joseph, M. R. Tomaszewski, I. Quiros-Gonzalez, J. Weber, J. Brunker, and S. E. Bohndiek, "Evaluation of Precision in Optoacoustic Tomography for Preclinical Imaging in Living Subjects," J. Nucl. Med. **58**(5), 807–814 (2017).

20. C. H. McCollough, M. R. Bruesewitz, M. F. McNitt-Gray, K. Bush, T. Ruckdeschel, J. T. Payne, J. A. Brink, and R. K. Zeman; American College of Radiology, "The phantom portion of the American College of Radiology (ACR) computed tomography (CT) accreditation program: practical tips, artifact examples, and pitfalls to avoid," Med. Phys. **31**(9), 2423–2442 (2004).

21. American College of Radiology, "Phantom test guidance for the ACR MRI accreditation program," http://www.acraccreditation.org/modalities/mri (22 December 2016).

22. ISO 80601–2-61:2017, "Medical electrical equipment–Part 2-61: Particular requirements for basic safety and essential performance of pulse oximeter equipment", Geneva, Switzerland (2017)

23. G. J. Tearney, E. Regar, T. Akasaka, T. Adriaenssens, P. Barlis, H. G. Bezerra, B. Bouma, N. Bruining, J. M. Cho, S. Chowdhary, M. A. Costa, R. de Silva, J. Dijkstra, C. Di Mario, D. Dudek, E. Falk, M. D. Feldman, P. Fitzgerald, H. M. Garcia-Garcia, N. Gonzalo, J. F. Granada, G. Guagliumi, N. R. Holm, Y. Honda, F. Ikeno, M. Kawasaki, J. Kochman, L. Koltowski, T. Kubo, T. Kume, H. Kyono, C. C. Lam, G. Lamouche, D. P. Lee, M. B. Leon, A. Maehara, O. Manfrini, G. S. Mintz, K. Mizuno, M. A. Morel, S. Nadkarni, H. Okura, H. Otake, A. Pietrasik, F. Prati, L. Räber, M. D. Radu, J. Rieber, M. Riga, A. Rollins, M. Rosenberg, V. Sirbu, P. W. Serruys, K. Shimada, T. Shinke, J. Shite, E. Siegel, S. Sonoda, M. Suter, S. Takarada, A. Tanaka, M. Terashima, T. Thim, S. Uemura, G. J. Ughi, H. M. van Beusekom, A. F. van der Steen, G. A. van Es, G. van Soest, R. Virmani, S. Waxman, N. J. Weissman, and G. Weisz; International Working Group for Intravascular Optical Coherence

Tomography (IWG-IVOCT), "Consensus standards for acquisition, measurement, and reporting of intravascular optical coherence tomography studies: a report from the International Working Group for Intravascular Optical Coherence Tomography Standardization and Validation," J. Am. Coll. Cardiol. **59**(12), 1058–1072 (2012).

24. ISO 16971:2015, "Ophthalmic instruments — Optical coherence tomograph for the posterior segment of the human eye", Geneva, Switzerland (2015)

25. S. Tzoumas, A. Nunes, I. Olefir, S. Stangl, P. Symvoulidis, S. Glasl, C. Bayer, G. Multhoff, and V. Ntziachristos, "Eigenspectra optoacoustic tomography achieves quantitative blood oxygenation imaging deep in tissues," Nat. Commun. **7**(1), 12121 (2016).

26. K. Daoudi, A. Hussain, E. Hondebrink, and W. Steenbergen, "Correcting photoacoustic signals for fluence variations using acousto-optic modulation," Opt. Express **20**(13), 14117–14129 (2012).

27. X. L. Deán-Ben, A. C. Stiel, Y. Jiang, V. Ntziachristos, G. G. Westmeyer, and D. Razansky, "Light fluence normalization in turbid tissues via temporally unmixed multispectral optoacoustic tomography," Opt. Lett. **40**(20), 4691–4694 (2015).

28. A. Q. Bauer, R. E. Nothdurft, T. N. Erpelding, L. V. Wang, and J. P. Culver, "Quantitative photoacoustic imaging: correcting for heterogeneous light fluence distributions using diffuse optical tomography," J. Biomed. Opt. **16**(9), 096016 (2011).

29. B. Cox, J. G. Laufer, S. R. Arridge, and P. C. Beard, "Quantitative spectroscopic photoacoustic imaging: a review," J. Biomed. Opt. **17**(6), 061202 (2012).

30. W. C. Vogt, C. Jia, K. A. Wear, B. S. Garra, and T. Joshua Pfefer, "Biologically relevant photoacoustic imaging phantoms with tunable optical and acoustic properties," J. Biomed. Opt. **21**(10), 101405 (2016).

31. W. C. Vogt, C. Jia, K. A. Wear, B. S. Garra, and T. J. Pfefer, "Phantom-based image quality test methods for photoacoustic imaging systems," J. Biomed. Opt. **22**(9), 1–14 (2017).

32. C. Jia, W. C. Vogt, K. A. Wear, T. J. Pfefer, and B. S. Garra, "Two-layer heterogeneous breast phantom for photoacoustic imaging," J. Biomed. Opt. **22**(10), 1–14 (2017).

33. L. G. Lindberg, M. Vegfors, C. Lennmarken, and P. A. Oberg, "Pulse oximeter signal at various blood flow conditions in an in vitro model," Med. Biol. Eng. Comput. **33**(1), 87–91 (1995).

34. C. D. Kurth, H. Liu, W. S. Thayer, and B. Chance, "A dynamic phantom brain model for near-infrared spectroscopy," Phys. Med. Biol. **40**(12), 2079–2092 (1995).

35. H. Wabnitz, A. Jelzow, M. Mazurenka, O. Steinkellner, R. Macdonald, D. Milej, N. Żołek, M. Kacprzak, P. Sawosz, R. Maniewski, A. Liebert, S. Magazov, J. Hebden, F. Martelli, P. Di Ninni, G. Zaccanti, A. Torricelli, D. Contini, R. Re, L. Zucchelli, L. Spinelli, R. Cubeddu, and A. Pifferi, "Performance assessment of time-domain optical brain imagers, part 2: nEUROPt protocol," J. Biomed. Opt. **19**(8), 086012 (2014).

36. S. Srinivasan, B. W. Pogue, S. Jiang, H. Dehghani, C. Kogel, S. Soho, J. J. Gibson, T. D. Tosteson, S. P. Poplack, and K. D. Paulsen, "Interpreting hemoglobin and water concentration, oxygen saturation, and scattering measured in vivo by near-infrared breast tomography," Proc. Natl. Acad. Sci. U.S.A. **100**(21), 12349–12354 (2003).

37. D. E. Myers, L. D. Anderson, R. P. Seifert, J. P. Ortner, C. E. Cooper, G. J. Beilman, and J. D. Mowlem, "Noninvasive method for measuring local hemoglobin oxygen saturation in tissue using wide gap second derivative near-infrared spectroscopy," J. Biomed. Opt. **10**(3), 034017 (2005).

38. S. Kleiser, N. Nasseri, B. Andresen, G. Greisen, and M. Wolf, "Comparison of tissue oximeters on a liquid phantom with adjustable optical properties," Biomed. Opt. Express **7**(8), 2973–2992 (2016).

39. J. R. Rajian, P. L. Carson, and X. Wang, "Quantitative photoacoustic measurement of tissue optical absorption spectrum aided by an optical contrast agent," Opt. Express **17**(6), 4879–4889 (2009).

40. J. Laufer, C. Elwell, D. Delpy, and P. Beard, "In vitro measurements of absolute blood oxygen saturation using pulsed near-infrared photoacoustic spectroscopy: accuracy and resolution," Phys. Med. Biol. **50**(18), 4409–4428 (2005).

41. Y. Jiang, A. Forbrich, T. Harrison, and R. J. Zemp, "Blood oxygen flux estimation with a combined photoacoustic and high-frequency ultrasound microscopy system: a phantom study," J. Biomed. Opt. **17**(3), 036012 (2012).

42. T. Mitcham, H. Taghavi, J. Long, C. Wood, D. Fuentes, W. Stefan, J. Ward, and R. Bouchard, "Photoacoustic-based sO$_2$ estimation through excised bovine prostate tissue with interstitial light delivery," Photoacoustics **7**, 47–56 (2017).

43. R. O. Esenaliev, I. V. Larina, K. V. Larin, D. J. Deyo, M. Motamedi, and D. S. Prough, "Optoacoustic technique for noninvasive monitoring of blood oxygenation: a feasibility study," Appl. Opt. **41**(22), 4722–4731 (2002).

44. H. K. Walker, W. D. Hall, and J. W. Hurst, *Clinical Methods: The History, Physical and Laboratory Examinations*, 3rd ed., Butterworth-Heinemann, St. Louis, MO (1990).

45. W. G. Zijlstra and A. Buursma, "Spectrophotometry of Hemoglobin: Absorption Spectra of Bovine Oxyhemoglobin, Deoxyhemoglobin, Carboxyhemoglobin, and Methemoglobin," Comp. Biochem. Physiol. B Biochem. Mol. Biol. **118**(4), 743–749 (1997).

46. W. C. Vogt, X. Zhou, R. Andriani, K. A. Wear, B. S. Garra, and J. Pfefer, "Performance evaluation of photoacoustic oximetry imaging systems using a dynamic blood flow phantom with tunable oxygen saturation," Proc. SPIE **10494**, 1049426 (2018).

47. J. R. Cook, R. R. Bouchard, and S. Y. Emelianov, "Tissue-mimicking phantoms for photoacoustic and ultrasonic imaging," Biomed. Opt. Express **2**(11), 3193–3206 (2011).

48. W. Xia, D. Piras, M. Heijblom, W. Steenbergen, T. G. van Leeuwen, and S. Manohar, "Poly(vinyl alcohol) gels as photoacoustic breast phantoms revisited," J. Biomed. Opt. **16**(7), 075002 (2011).

49. E. Maneas, W. Xia, O. Ogunlade, M. Fonseca, D. I. Nikitichev, A. L. David, S. J. West, S. Ourselin, J. C. Hebden, T. Vercauteren, and A. E. Desjardins, "Gel wax-based tissue-mimicking phantoms for multispectral photoacoustic imaging," Biomed. Opt. Express **9**(3), 1151–1163 (2018).

50. S. A. Prahl, M. J. C. van Gemert, and A. J. Welch, "Determining the optical properties of turbid mediaby using the adding-doubling method," Appl. Opt. **32**(4), 559–568 (1993).

51. A. Pifferi, J. Swartling, E. Chikoidze, A. Torricelli, P. Taroni, A. Bassi, S. Andersson-Engels, and R. Cubeddu, "Spectroscopic time-resolved diffuse reflectance and transmittance measurements of the female breast at different interfiber distances," J. Biomed. Opt. **9**(6), 1143–1151 (2004).

52. H. J. van Staveren, C. J. Moes, J. van Marie, S. A. Prahl, and M. J. van Gemert, "Light scattering in Intralipid-10% in the wavelength range of 400-1100 nm," Appl. Opt. **30**(31), 4507–4514 (1991).

53. ANSI Z136.1:2014, "American National Standard for Safe Use of Lasers", Laser Institute of America, Orlando, Florida (2014)

54. S. A. Carp, S. A. Prahl, and V. Venugopalan, "Radiative transport in the delta-P1 approximation: accuracy of fluence rate and optical penetration depth predictions in turbid semi-infinite media," J. Biomed. Opt. **9**(3), 632–647 (2004).

55. N. Bosschaart, G. J. Edelman, M. C. G. Aalders, T. G. van Leeuwen, and D. J. Faber, "A literature review and novel theoretical approach on the optical properties of whole blood," Lasers Med. Sci. **29**(2), 453–479 (2014).

56. F. B. Jensen, "Red blood cell pH, the Bohr effect, and other oxygenation-linked phenomena in blood O2 and CO2 transport," Acta Physiol. Scand. **182**(3), 215–227 (2004).

57. G. P. Luke and S. Y. Emelianov, "Optimization of in vivo spectroscopic photoacoustic imaging by smart optical wavelength selection," Opt. Lett. **39**(7), 2214–2217 (2014).

58. G. Held, S. Preisser, H. G. Akarçay, S. Peeters, M. Frenz, and M. Jaeger, "Effect of irradiation distance on image contrast in epi-optoacoustic imaging of human volunteers," Biomed. Opt. Express **5**(11), 3765–3780 (2014).

59. K. Daoudi, P. J. van den Berg, O. Rabot, A. Kohl, S. Tisserand, P. Brands, and W. Steenbergen, "Handheld probe integrating laser diode and ultrasound transducer array for ultrasound/photoacoustic dual modality imaging," Opt. Express **22**(21), 26365–26374 (2014).

60. G. S. Sangha, N. J. Hale, and C. J. Goergen, "Adjustable photoacoustic tomography probe improves light delivery and image quality," Photoacoustics **12**, 6–13 (2018).

61. M. W. Schellenberg and H. K. Hunt, "Hand-held optoacoustic imaging: A review," Photoacoustics **11**, 14–27 (2018).